A&A 632, A47 (2019)
https://doi.org/10.1051/0004-6361/201935271

Astronomy & Astrophysics

PACT

I. Combining ACT and *Planck* data for improved extraction of tSZ signal

N. Aghanim[1], M. Douspis[1], G. Hurier[2], D. Crichton[3], J.-M. Diego[4], M. Hasselfield[5,6], J. Macias-Perez[7], T. A. Marriage[8], E. Pointecouteau[9], M. Remazeilles[10], and E. Soubrié[1]

[1] Institut d'Astrophysique Spatiale, CNRS (UMR8617) Université Paris Sud, Bâtiment 121, Orsay, France
e-mail: nabila.aghanim@ias.u-psud.fr
[2] Centro de Estudios de Física del Cosmos de Aragón (CEFCA), Plaza de San Juan, 1, Planta 2, 44001 Teruel, Spain
[3] Astrophysics and Cosmology Research Unit, School of Mathematics, Statistics and Computer Science, University of KwaZulu-Natal, Durban 4041, South Africa
[4] Instituto de Física de Cantabria (CSIC-UC), Avda. Los Castros s/n, 39005 Santander, Spain
[5] Department of Astronomy and Astrophysics, The Pennsylvania State University, University Park, PA 16802, USA
[6] Institute for Gravitation and the Cosmos, The Pennsylvania State University, University Park, PA 16802, USA
[7] LPSC, Université Joseph Fourier Grenoble 1, CNRS/IN2P3, Institut National Polytechnique de Grenoble, 53 Av. des Martyrs, 38026 Grenoble, France
[8] Dept. of Physics and Astronomy, Johns Hopkins University, 3400 N. Charles St., Baltimore, MD 21218, USA
[9] IRAP, Université de Toulouse, CNRS, CNES, UPS, Toulouse, France
[10] Jodrell Bank Centre for Astrophysics, School of Physics and Astronomy, The University of Manchester, Manchester M13 9PL, UK

Received 14 February 2019 / Accepted 16 May 2019

ABSTRACT

We present the optimal reconstruction of the thermal Sunyaev–Zel'dovich (tSZ) effect signal based on the combination of a heterogeneous dataset consisting of Atacama Cosmology Telescope (ACT) and *Planck* data, with different numbers of channels, angular resolutions, and noise levels. We combine both datasets using two different approaches, a matched multifilter (MMF) technique and an optimized internal linear combination (ILC). We show that when applying the MMF to the combination of ACT and *Planck* data, the size-flux degeneracy is reduced and the signal-to-noise of clusters detected with their Sunyaev–Zel'dovich (SZ) signal improves by up to a factor of three. In the case of the optimized ILC method, we show that the tSZ map is reconstructed with a resolution of ∼1.5 arcmin. This is more than a factor two improvement compared with the *Planck* resolution, and with a very good control of noise, meaning that it is limited only by the intrinsic noise of the individual experiments. The combination of ACT and *Planck* data offers a unique opportunity to improve on the study of the pressure profiles and to study substructure in clusters through their tSZ.

Key words. cosmic background radiation – cosmology: observations – galaxies: clusters: general – methods: data analysis

1. Introduction

The thermal Sunyaev–Zel'dovich (tSZ) effect is a spectral distortion of the cosmic microwave background (CMB) blackbody radiation due to inverse Compton scattering of the CMB photons by hot electrons contained in the intra-cluster gas (Zeldovich & Sunyaev 1969; Birkinshaw 1999). In the nonrelativistic approximation, the tSZ effect has a distinctive frequency signature independent of redshift. Furthermore, for clusters of galaxies (dominant contribution to the tSZ signal) there is also a distinctive spatial distribution associated with their pressure profile, which translates into a dependency in the angular power-spectrum of the tSZ. The microwave sky is the result of several astrophysical and cosmological signals that include the CMB; foreground emission from the Galactic interstellar medium; the cosmic infrared background (CIB) emission; the emission from compact extra-galactic radio sources; and the aforementioned tSZ. These signals typically have both distinctive frequency signatures and spatial distribution in the sky. In addition to these foregrounds, observations also include instrumental noise. Separating the different astrophysical and cosmological components is a challenging task, but in general, this separation improves when more frequencies are added into the reconstruction method.

Thanks to the recent CMB surveys by the Atacama Cosmology Telescope (ACT; Marriage et al. 2011; Hasselfield et al. 2013a; Hilton et al. 2018), South Pole Telescope (SPT; Staniszewski et al. 2009; Bleem et al. 2015), and *Planck* (Planck Collaboration I 2018, and references therein), wide-field multi-frequency data are now available for tSZ studies. These surveys differ notably in terms of their numbers of frequency channels and in terms of their angular resolutions from ∼1.5 arcmin for ground-based surveys to ∼5 arcmin for the highest *Planck* frequencies. Also, the noise properties can vary significantly, especially for the ground-based experiments, where changes in the atmospheric conditions can result in spatial variations at large angular scales. In this context, reconstruction of the tSZ signal relies on our capacity to optimally combine the available multi-frequency and multi-instrument data.

Several component separation methods have been successfully used in the *Planck* context (e.g., Bobin et al. 2008; Remazeilles et al. 2011; Hurier et al. 2013). In Remazeilles et al. (2013) a first study based on simulated data showed that

joint exploitation of multiple experiments producing heterogeneous data is possible. The needlet internal linear combination (ILC) method used in Remazeilles et al. (2013) efficiently aggregates simulated ACT-like and *Planck*-like data to construct high-resolution tSZ patch-maps around clusters of galaxies. The first combination of data from multiple heterogeneous CMB experiments to produce an optimal temperature map was performed by Bobin et al. (2014, 2016) using the *Planck* and Wilkinson Microwave Anisotropy Probe data. A more recent study by Chown et al. (2018) produced a CMB map from the linear combination of SPT and *Planck* data. *Planck* and SPT data were also combined to produce maps of the Magellanic Clouds (Crawford et al. 2016).

In this paper, we present the first optimal reconstruction of the tSZ effect signal based on the combination of publicly available ACT and *Planck* data. The combination, based on an ILC approach, takes advantage of the complementarity between the two experiments: the higher resolution of ACT to detect compact tSZ clusters and characterize pressure profiles on smaller, angular scales and the larger number of frequencies and measurement stability of *Planck* to clean the foreground contamination and CMB, and allow access to larger angular scales filtered out in ground experiments. The paper is organized as follows. In Sect. 2, we provide a brief description of the data used. We then present two ways of combining ACT and *Planck* data – the matched multifilter used to optimally detect clusters of galaxies and the ILC method to reconstruct a tSZ map, in Sect. 3. The results in terms of the tSZ radial profile, significance of tSZ detection, and size-flux measurement for clusters are reported in Sect. 4. We conclude in Sect. 5.

2. Data

We focus on two CMB surveys, ACT and *Planck*, which differ by their angular resolutions, by their available frequency channels, and by their sky coverage. In the following, both datasets are considered as a single composite dataset of intensity and associated noise maps. Characteristics of the maps from both experiments are summarized in Table 1. We performed our analysis using this composite multi-instrument data that will be referred to as the PACT dataset in the rest of the paper.

We used the publicly available total intensity dataset of the High Frequency Instrument (HFI) taken during the full mission of the *Planck* survey, meaning the six highest-frequency *Planck* channel maps, from 100 to 857 GHz at native resolution (Planck Collaboration VIII 2016). The full *Planck* datasets are available at the *Planck* Legacy Archive (PLA)[1]. A noise map is associated with each channel map and is constructed from the difference of the first half and second half of the *Planck* rings for a given pointing position of the satellite spin axis. These maps are mainly free from astrophysical emission and they are considered a good representation of the statistical instrumental noise (Planck Collaboration VIII 2016). As the goal of this work is to focus on the Sunyaev–Zel'dovich (SZ) signal, in addition to the intensity maps we also use publicly available mask maps constructed to remove regions of the sky affected by point sources and strong galactic emission, also available at PLA. The *Planck* PR3 data show an improved estimate of the dipolar component consecutive to the improved calibration. This translates into an improved estimate of the signal for the largest angular scales, which does not impact the analysis of the PACT data that cover only a small fraction of the sky. Furthermore, the intercalibration between frequencies (which is a key quantity for the tSZ measurements) is the same as that of PR2, namely better than 1%. As a results and despite the improved, large-scale calibration of PR3, we chose to use the PR2 dataset, also including a tSZ catalog and a tSZ map, used to compare with our results.

Table 1. *Planck* and ACT frequencies, beams and SZ conversion factors.

	Frequency [GHz]	$FWHM$ [arcmin]	$g(\nu)\,T_{\rm CMB}$ [$K_{\rm CMB}$]
Planck	100	9.68	−4.03121
	143	7.30	−2.78564
	217	5.02	0.18763
	353	4.94	6.20518
	545	4.83	14.45559
	857	4.64	26.33521
ACT	148	1.374	−2.69100
	220	1.053	0.10400

Notes. The conversion factors are computed without relativistic corrections.

We used *Planck* circular Gaussian beams with full width half maximum (FWHM) values from (Planck Collaboration VII 2016, Table 3) and the values provided in Planck Collaboration XXII (2016) for the tSZ transmission in *Planck* spectral bandpasses. To allow a direct combination of *Planck* and ACT datasets, all *Planck* maps were projected into the world coordinate system of the 148 GHz ACT map.

For the ACT dataset, we used the publicly available 148 and 220 GHz data in the southern and equatorial areas at native resolution 1–1.4 arcmin. The ACT data are the "raw" frequency maps and were not processed further beyond that described in this paper. They were collected from 2008–2010 using the Millimeter Bolometric Array Camera (Swetz et al. 2011). The ACT data reduction is described in Dünner et al. (2013). We also used the associated weight maps and point-source masks[2]. The latter are defined to be zero in a 5 arcmin circle at the location of sources detected with flux density greater than 15 mJy at 148 GHz[3]. Finally, we used the beam characteristics and tSZ transmission band centers in Hasselfield et al. (2013b) and Swetz et al. (2011), respectively.

In the following, we combined the full ACT dataset with the overlapping *Planck* coverage. However, we identified two deeper regions that are used to illustrate the results, called $S_{\rm deep}$ and $E_{\rm deep}$ for the southern and equatorial regions, respectively. These selected areas are displayed as black rectangles in Fig. 3. The area $S_{\rm deep}$ is defined such that $56.3° < {\rm RA} < 97.9°$ and $-55.3° < {\rm Dec} < -51.2°$. The area $E_{\rm deep}$ is such that $4.1° < {\rm RA} < 53.6°$ and $-1.06° < {\rm Dec} < 1.40°$. In order to combine *Planck* and ACT maps, we remapped *Planck* native NSIDE=2048 Healpix data onto ACT's native (square) 0.5′ pixels. The remapping was performed after adopting an auxiliary pixel scale with a size 4×4 times smaller than the ACT pixel. The small pixel scale allows us to properly account for pixel mixing by weighting the portion of the *Planck* Healpix pixel that overlaps with the ACT pixel. At most, four Healpix pixels overlap partially with one ACT pixel. The final

[1] http://www.sciops.esa.int

[2] All ACT data products can be found at the Legacy Archive for Microwave Background Data (https://lambda.gsfc.nasa.gov/).

[3] Note that no source detection was performed in the 18-hour field of the Southern area.

value assigned to the ACT pixel is a linear combination of the intensities in these four pixels, with weights proportional to the area fraction that overlaps with the ACT pixel. In most cases, only one of the weights is non-zero. We investigated an alternative remapping of the *Planck* data onto the ACT pixelization. First the native *Planck* data were projected onto the ACT pixels with a cylindrical, equal-area, world coordinate system. The projected data were then Fourier transformed and filtered with an isotropic function that takes the value of unity in the range $2 < \ell < 5000$ and decreases smoothly as a cosine to zero at $\ell = 10\,000$. This Fourier-based interpolation removes the artificial Healpix pixel edges and retains the information present in the *Planck* data. We verified that results are independent of the remapping method, and finally show the results from the remapping based on finer ACT pixels.

3. Combining ACT and *Planck* data

In this section, we present two different approaches for the combination of the ACT and *Planck* datasets, both optimized for the tSZ studies. The first one consists in combining the ACT and *Planck* maps through an MMF technique. This method is particularly optimized for the detection of tSZ sources and the measurement of their significance and photometry. The second approach consists in reconstructing a tSZ y-map using an ILC method to combine the frequency maps of the PACT dataset.

In Sect. 4 we show some of the advantages of the PACT dataset over the individual *Planck* and ACT data. Full analyses of the tSZ source catalog and y-map derived from the PACT dataset are beyond the scope of the present study. Hence as a proof of concept, we focused mostly on the deepest region of the ACT data, $S_{\rm deep}$, and we illustrate our results and compare them with those obtained, for the same region, by *Planck* and ACT separately.

3.1. MMF for PACT data

Several methods geared toward the detection of tSZ clusters were proposed in the literature. MMF techniques (e.g., Herranz et al. 2002; Melin et al. 2006; Carvalho et al. 2009, and references therein) have been successfully used in the context of both single and multifrequency CMB surveys such as ACT, SPT, and *Planck*. Large and complementary catalogs of galaxy clusters were produced in these surverys[4].

The power of the MMF technique resides in the fact that it enhances the signal-to-noise ratio (S/N) of a tSZ source by optimally filtering a set of multifrequency sky maps containing an ensemble of contaminating signals (e.g., galactic dust, CMB, etc.). The optimal filtering of the tSZ signal is achieved thanks to two characteristics. On the one hand, the tSZ spectral signature is assumed to be known and universal, as far as the electrons of the intracluster medium are nonrelativistic. On the other hand, the tSZ cluster signal is described by a spatial template following a projected, spherical generalized Navarro–Frenk–White (NFW) profile (Arnaud et al. 2010) characterized by a single parameter: a characteristic radius $\theta_{\rm s}$. The optimal filter defined this way reduces both the foreground contamination and the instrumental noise, using a linear combination of the frequency maps.

Being a detection method based on matched filters for multiple frequency data, the MMF is particularly well-adapted for the combination of the ACT and *Planck* data. In the present study, we used all six frequency maps from the *Planck*-HFI instrument and the ACT frequency maps together with the associated noise maps at their native resolutions.

In practice, the MMF technique consists in filtering the maps with optimal spatial and spectral filters derived from prior knowledge on clusters. We assumed the generalized NFW profile (Nagai et al. 2007; Arnaud et al. 2010) to describe the spatial pressure distribution and a nonrelativistic tSZ signature for the spectral dependency. The properties (size θ, flux Y, S/N) of each cluster can be computed by maximising the following S/N (see Melin et al. 2006; Carvalho et al. 2012, for detail):

$$S/N(\theta) = \frac{\hat{Y}}{\sigma}(\theta) = \frac{\int \mathrm{d}x^2 \boldsymbol{F}_\theta(x - x_0) \cdot \boldsymbol{M}(\boldsymbol{x})}{\sigma_\theta} \quad (1)$$

where the operation is done in Fourier space on the maps $\boldsymbol{M}$, with:

$$\boldsymbol{F}_\theta(x) = \sigma_\theta^2 \boldsymbol{P^{-1}}(\boldsymbol{k}) T_{\theta,\nu}. \quad (2)$$

We performed the MMF analysis using the eight available frequency maps in the PACT dataset (*Planck*-HFI: $\nu = 100$, 143, 217, 353, 545, 857 GHz, and ACT: $\nu = 148$, 220 GHz). $P^{-1}(k)$ is thus the 8×8 power spectrum map of the maps and T is the spatial templates of the cluster with different sizes θ weighted by the tSZ spectral signature.

The noise can be computed from the power spectrum of the maps with:

$$\sigma_\theta = \left[\int \mathrm{d}^2 k \; \boldsymbol{T}^t_{\boldsymbol{\theta},\boldsymbol{\nu}}(\boldsymbol{k}) \cdot \boldsymbol{P}^{-1} \cdot \boldsymbol{T}_{\boldsymbol{\theta},\boldsymbol{\nu}}(\boldsymbol{k}) \right]^{-1/2}. \quad (3)$$

The MMF is specifically designed to reduce the foreground contamination however it was shown in Planck Collaboration VIII (2011), Planck Collaboration XXIX (2014), Planck Collaboration Int. XXXII (2015) and Planck Collaboration XXVII (2016) that spurious SZ sources can be associated with IR emission from cold galactic clumps or other point-like sources. Many strategies can be followed in order to clean the tSZ detections of spurious sources such as cross-matching with external cluster catalogs, comparison with galaxy surveys, or statistically-based classification (Aghanim et al. 2015). At the same time, one can attempt to reduce the possible contamination at an earlier stage of the analysis. To do so, we applied a mask for point sources consisting in the union of the *Planck* and ACT point-sources masks (presented in Sect. 2) to the ensemble of PACT frequency maps before their analysis. The PACT dataset, that is all *Planck*-HFI and ACT channel maps, was then processed with an MMF filter. For this, the size of the spatial template is varied between 0.1 and 50 arcmin in 50 logarithmically spaced bins. A detected tSZ source is defined as the one with the highest S/N when varying the template size. The associated size and flux measured from the filter are defined as the ones of detected source.

It is beyond the scope of the present study to construct and deliver a catalog of clusters and tSZ sources from the PACT dataset. Our aim is to show the complementarity and added value of combining ACT and *Planck* data. We thus illustrate the application of the MMF to the detection of the tSZ sources in the combined PACT dataset by focusing on results of the deep region $S_{\rm deep}$. Furthermore, we verified that neither S/N nor tSZ fluxes derived from the MMF method are improved when we use both the 148 and the 220 GHz ACT maps or only the 148 GHz map. We therefore choose to show the results of the analysis using all

[4] A meta-catalog collecting all the catalog entries of these individual experiments is available at http://szcluster-db.ias.u-psud.fr/

eight frequency channels of the PACT dataset (two from ACT and six from *Planck*).

In this configuration, we detect in total 58 tSZ sources above a threshold of $S/N = 4.3$. This threshold corresponds to the lowest S/N of the tSZ sources identified with actual clusters (i.e., below $S/N = 4.3$ the tSZ sources are either candidate tSZ clusters or spurious detections). The sample of 58 tSZ PACT sources contains 22 actual clusters. The identification of counterparts was performed by searching for already-known clusters from tSZ, X-ray, and optical catalogs in a 5 arcmin radius around the position of the PACT detected tSZ sources. We used the tSZ compilation of 2690 tSZ sources[5]. We also used the meta-catalog of X-ray detected clusters (Piffaretti et al. 2011). In the optical, we used catalogs from the Sloan Digital Sky Survey survey (Rykoff et al. 2014; Wen & Han 2015). Finally, we queried the NASA/IPAC extragalactic database for the PACT sources that are not associated with known clusters.

Thanks to the optimal combination of the ACT and *Planck* data with the MMF, we are able to recover all the clusters detected by ACT and *Planck* not only those common to both experiments but also those detected independently by ACT or by *Planck*. This amounts to 14 clusters of galaxies in total. Furthermore, all *Planck* clusters recovered from the PACT data have $S/N > 4.5$, which is the *Planck* detection threshold. Below we discuss the improvement in S/N due to the PACT combination of data. The improvement brought by the PACT dataset can also be seen in the detection of eight new tSZ sources in the $S_{\rm deep}$ region associated with actual clusters from optical, X-ray, or tSZ catalogs. Their redshifts range from $z = 0.21$ to 0.93. Thanks to the PACT dataset and combining ACT's high resolution and *Planck*'s cleaning capabilities, we detect clusters at $z \simeq 0.9$ that were reported neither in the ACT nor in the *Planck* catalogs. This illustrates the potential of the PACT data for high redshift clusters.

3.2. PACT y-map construction

We combined the *Planck* and ACT data to build a joint tSZ y-map, called the PACT y-map. As described in Remazeilles et al. (2013), such a combination can be performed using component separation techniques that aggregate the data. We choose here to illustrate the results for the modified internal linear combination algorithm (MILCA) method (see Hurier et al. 2013 for details).

The MILCA method allowed us to perform a scale-dependent optimization of the reconstructed tSZ signal with respect to noise and foreground residuals for all of the equatorial and southern regions covered both by ACT and *Planck*. Figure 1 shows the resulting reconstructed y-map in a selected area of the PACT footprint.

MILCA is a semiblind, multiscale component separation method allowing us to reconstruct a given sky emission from the weighted average of the input sky maps. In the case of the tSZ emission from clusters, MILCA requires an input of mainly the tSZ spectral dependence, although additional constraints can be considered to optimize the separation. In the present case, we used a second spectral constraint to suppress the CMB contribution in the reconstructed y-map at large scale. This is possible thanks to the use of the multifrequency sky maps of *Planck*. At small scale (below 5 arcmin), due to the poor resolution of the *Planck* maps the relevant signal is obtained from the ACT-148 GHz map, and thus the CMB emission can not be spectrally separated from the tSZ emission of the clusters. However, at such small angular scales CMB primary temperature anisotropies can be neglected with respect to the expected tSZ decrement on clusters at 148 GHz. Similarly, contamination by infrared and radio point sources cannot be suppressed at very small scales. They thus produce respectively spurious positive and negative sources in the MILCA-produced PACT y-map.

Assuming that the observed sky emission $M_\nu^{\rm obs}$ at each of the frequency bands ν of *Planck* and ACT can be written as the linear combination of various independent sky emission components S^c with spectral laws f_ν^c:

$$M_\nu^{\rm obs} = \sum_c f_\nu^c \, S^c, \tag{4}$$

while the MILCA estimator reads:

$$\boldsymbol{M}_{\rm MILCA} = \left[\boldsymbol{F}^{\rm T} C_{\boldsymbol{T}^{-1}} \boldsymbol{F}\right]^{-1} \boldsymbol{F}^{\rm T} C_{\boldsymbol{T}^{-1}} \boldsymbol{T}, \tag{5}$$

$\boldsymbol{M}_{\rm MILCA}$ being the MILCA reconstructed sky maps, and S^c corresponding to the imposed spectral constraints in this case tSZ and CMB. $\boldsymbol{F}$ is a vector containing the spectral constraints for the tSZ and CMB components. $\boldsymbol{T}$ is a vector containing the input sky maps, $M_\nu^{\rm obs}$ from *Planck* and ACT at the different frequency bands, and $C_{\boldsymbol{T}}$ is the covariance matrix for the sky maps per frequency. Additionally, we used a rank reduction approach on $C_{\boldsymbol{T}}$ over three degrees of freedom and the instrumental noise over the last two degrees of freedom in order to minimize the contribution from other astrophysical emissions (see, Hurier et al. 2013, for a detailed description of this procedure).

In Fig. 2, we show the relative contribution, meaning weight from each of the seven channel or intensity maps to the PACT y-map. We do not include the 220 GHz channel from ACT in the reconstruction of the tSZ map by MILCA since it improves the statistical noise only very slightly by about 1%, whereas it introduces correlated noise from sky background, which is more difficult to model and thus to control. The weights show that ACT and *Planck* experiments complement each other nicely and that their combination allows us to take advantage of *Planck* data at scales below $\sim$0.1 arcmin^{-1} and ACT data above, as discussed below. The 148 GHz map from ACT (the thick, solid gray line) dominates the contribution to the PACT y-map at scales above ~ 0.1 arcmin^{-1} due to the higher ACT resolution.

We note that most of the contribution to the tSZ signal at large, angular scales in the PACT y-map reconstruction actually comes from the *Planck* frequency channels with large beams. Since they dominate the cleaning from foregrounds in the MILCA method (and more generally in ILC approaches). Figure 2 highlights the dominant contributions to the PACT y-map from the 143 and 353 GHz channels at large scales. It also shows that the highest frequency, 857 GHz, tracing the Galactic dust emission does not contribute significantly to the reconstruction of the tSZ map. The two highest frequencies, 545 and 857 GHz, are however essential for thermal dust-emission removal. Considering that the sky is completely dominated by the thermal dust emission at these frequencies, and in particular at 857 GHz, only a small weight is needed for the reconstruction of the tSZ signal.

We produced a reconstructed PACT y-map from the combination of seven frequency maps, corresponding to the six *Planck* highest-frequency channels and the 148 GHz channel from ACT. Adding the 220 GHz channel from ACT did not improve the final results. This channel can be more subject to contamination by atmospheric emission, whose large-scale features increase the

[5] It is based on the catalogs from *Planck*, ACT, SPT, CARMA, AMI. The meta-catalog is available at http://szcluster-db.ias.u-psud.fr/

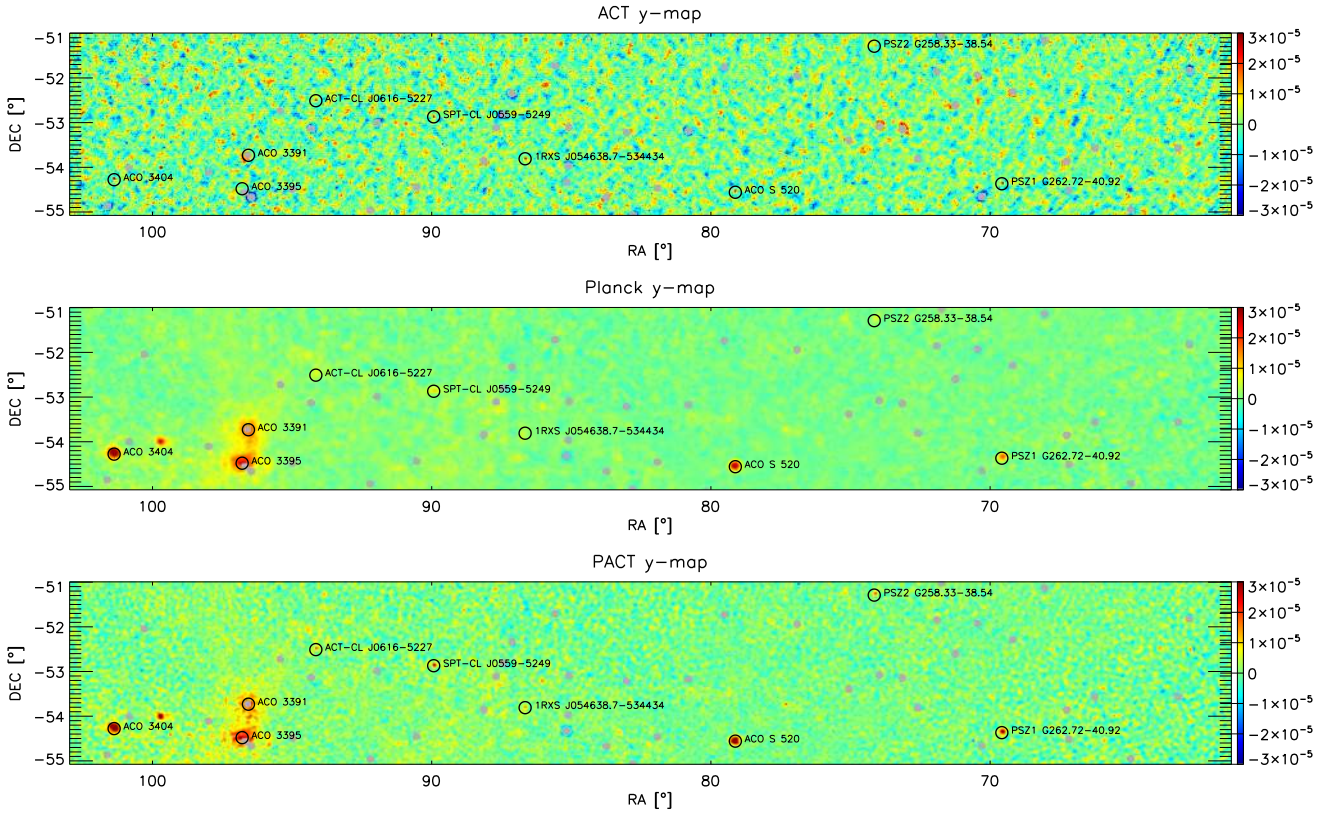

Fig. 1. Maps of unitless (color bar) Compton y parameter illustrated on selected southern ACT area. *Top panel*: 148 GHz-ACT map at 1.5 arcmin resolution with scales larger than 7 arcmin filtered out. *Middle panel*: *Planck* y-map reconstructed with a modified internal linear component algorithm (MILCA) at 7 arcmin resolution. *Lower panel*: PACT y-map reconstructed with MILCA at 3 arcmin resolution. Circles indicate some known clusters in the selected area. The ACT point sources are masked in all three panels (gray areas).

noise level in the MILCA reconstruction (MMF is less sensitive to such systematics due to the filtering step). Therefore,we chose to discard the 220 GHz from the MILCA reconstruction of the y-map. In the bottom panel of Fig. 1, we show the resulting y-map in the $S_{\rm deep}$ area. For the same region, the *Planck* y-map and the 148 GHz-ACT map are displayed in the top and middle panels in units of Compton parameter, respectively. We clearly notice the lack of signal at large scales in the ACT y-map. This is due to the high-pass filtering at 7 arcmin applied to enhance tSZ-scale signal. The 148 GHz-ACT map given in units of Compton parameter (hereafter ACT y-map) also exhibits some radio-source contamination mainly shown as a negative signal. We note that the counterpart of the brightest radio-source in the ACT y-maps displays a positive ring introduced by the MILCA multiscale reconstruction that uses the various frequencies with different relative weights due to their different angular resolutions (see Fig. 2). The *Planck* y-map shows large-scale tSZ scale signal due to the larger *Planck* beams. It also shows contamination from radio-sources at a lower amplitude than ACT y-map, due both to the large frequency coverage, which eases the component separation, and to the beam smearing. If we now turn to the PACT y-map (Fig. 1 bottom panel), we see the advantages of combining the two experiments into a single dataset with MILCA. As seen in the area of the pair of clusters A3395–A3391, we do recover the large angular scales in the PACT y-map thanks to *Planck*. We also clearly see the improvement brought by the higher resolution of ACT both in terms of spatial structure and in terms of significance. This is seen on the two *Planck* clusters in the field PSZ1 G258.33−38.54 and PSZ2 G262.72−40.92. Finally, the advantage of the combination of ACT and *Planck*

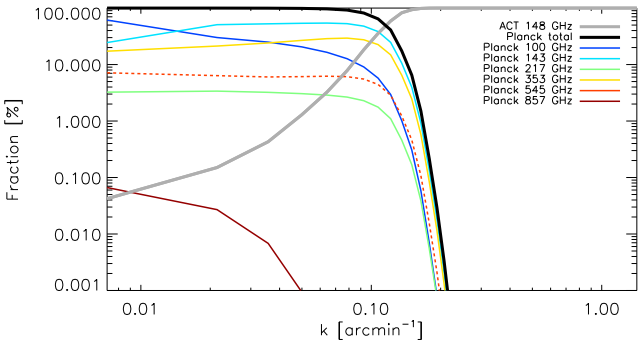

Fig. 2. Relative contribution, i.e., weights, as a function of scales to reconstructed PACT y-map of each frequency channel. Shown are 100 GHz in dark blue, 143 GHz in light blue, 148 GHz in gray, 217 GHz in green, 353 GHz in yellow, 545 GHz in red, and 857 GHz in brown. The relative contribution to the reconstructed PACT y-map from *Planck* is shown as thick black line.

is also illustrated by the detection of a higher number of tSZ sources seen as positive sources in the y-map (including actual clusters not detected independently by ACT or by *Planck*). The PACT reconstructed y-map also shows contamination by radio-sources, which can be easily mitigated thanks to their negative signal.

The noise map of the PACT shown in Fig. 3 is obtained from the half-dataset difference maps and by applying the same linear combination (and weights) as the one used to compute the reconstructed PACT y-map. The PACT noise maps in Fig. 3

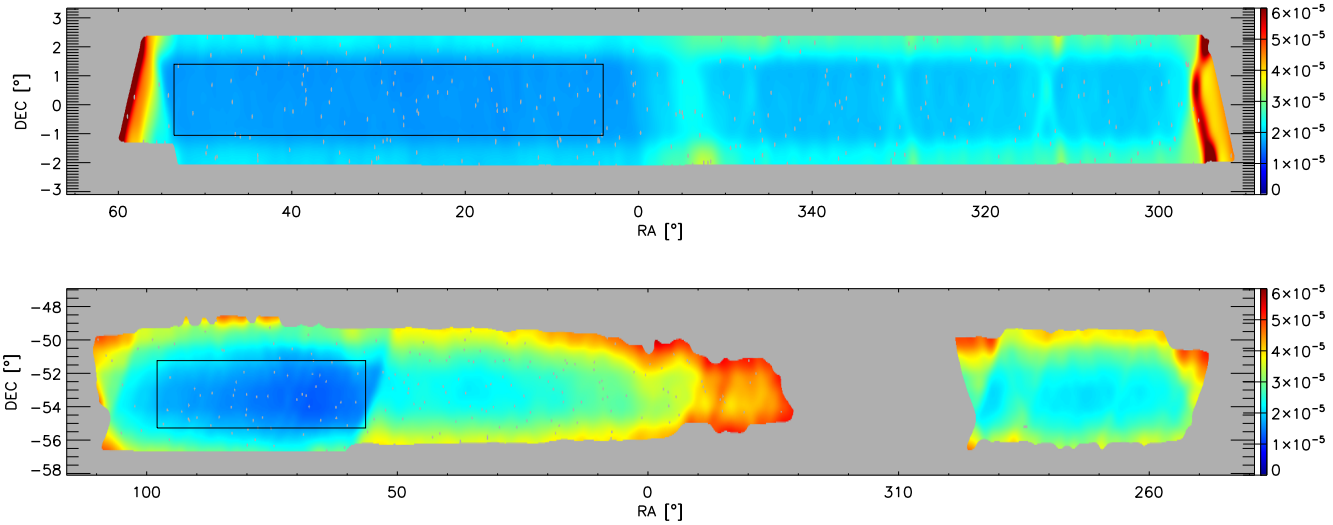

Fig. 3. Combined noise maps in native ACT resolution of 1.4 arcmin, overlaid with ACT point-source masks. The color bar represents the unitless Compton y parameter. *Top*: ACT equatorial area. *Bottom*: ACT southern area. The rectangle in each panel represents the deepest area $S_{\rm deep}$ (in the southern region) and $E_{\rm deep}$ (in the equatorial region).

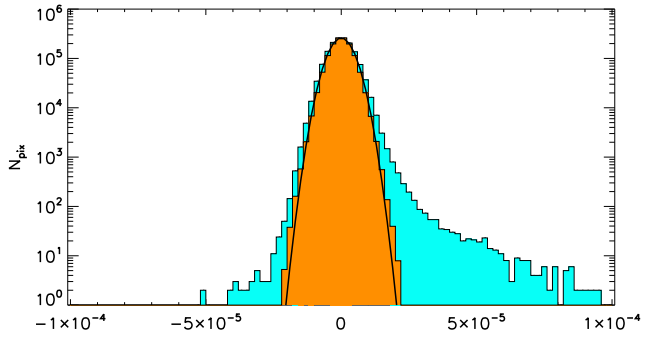

Fig. 4. Distribution of pixels for MILCA PACT y-map. The tSZ signal is shown in light blue, and the noise is shown in orange. The solid black line shows a Gaussian fit adjusted to the noise distribution.

are shown for the ACT equatorial footprint (top panel) and southern footprint (bottom panel). The rectangular regions represent selected deep regions defined in Sect. 2. By construction of the PACT dataset from the combination of ACT and *Planck* frequency channels, the associated noise structures are scale dependent. This is exhibited in the bottom panel of Fig. 1 where we note that the spatial distribution of noise is correlated and inhomogeneous, considering that large, angular scales are dominated by *Planck* data and small, angular scales by ACT data.

To illustrate the quality of the PACT MILCA tSZ y-map, in Fig. 4 we present S/N of tSZ in the pixel distribution of both PACT maps. The noise is well approximated by a Gaussian distribution whereas the distribution of tSZ signal exhibits a non-Gaussian distribution with an notable positive tail and a smaller negative tail. Only considering the negative pixels in the PACT y-map, the background standard deviation is 4.6×10^{-6} in Compton parameter units. The statistical noise contributes 4.0×10^{-6} to the standard deviation background of the PACT y-map. Thus, other sources of background fluctuations account for $\simeq2.3\times10^{-6}$. This additional contribution is likely produced by residual astrophysical emissions such as individual sources and CIB. The CIB residuals in the tSZ maps at large scale is mainly Gaussian (see, Planck Collaboration XXIII 2016). However, at small scales the PACT map is dominated by the contribution from the 148 GHz channel in which the CIB conserves all its complexity and non-Gaussian characteristics.

Finally, we computed and show the power spectra of the *Planck*, ACT and PACT y-map and of the associated noise map in Fig. 5. The small-scale noise spectrum, above $k \sim 0.2\,\mathrm{arcmin}^{-1}$, is dominated by that of ACT, as was expected. The feature at $\sim0.3\,\mathrm{arcmin}^{-1}$ in the southern PACT signal power-spectrum is associated with the stripes in the ACT 148 GHz signal map translated into oscillation in the power spectrum that are propagated to the PACT power-spectrum. At larger scales, the noise spectrum is dominated by *Planck* with an amplitude slightly larger than the ACT noise in the southern area and significantly larger in the equatorial region due to the *Planck* scanning-strategy, with lower redundancy (and hence higher noise) in the equatorial region. We observe a large bump around $0.1\,\mathrm{arcmin}^{-1}$ that reflects the angular scales where the contribution to the tSZ signal transits from ACT to *Planck*. In the southern area, we note that the tSZ signal exhibits a clear excess of power compared to the noise power-spectrum. This signal includes contributions from tSZ, CIB, and point sources (see, Planck Collaboration XXI 2014, for a detailed analysis of the tSZ power-spectrum).

4. Properties of the tSZ clusters from the PACT dataset

The combination of the ACT and *Planck* data into the PACT dataset improves the yield of detected tSZ sources as discussed in Sect. 3.1. It also improves the quality of the reconstructed y-map as seen in Sect. 3.2. We now show the improvements brought by the ACT and *Planck* combination by focusing on three aspects: the significance of the tSZ clusters detected by ACT or *Planck*, namely their S/N; their estimated flux and sizes; and finally the Compton parameter profile.

4.1. Sample description

We focused on a union sample of 119 galaxy clusters detected either by *Planck* or by ACT. We used the ACT catalog

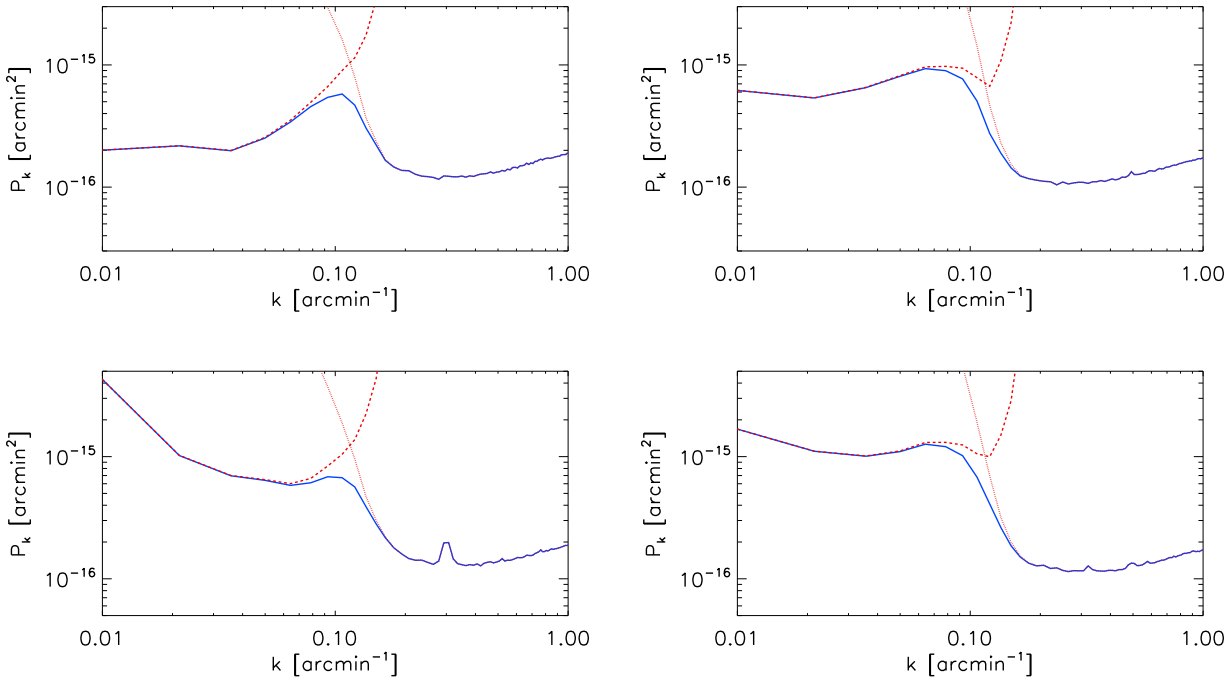

Fig. 5. S/N of tSZ in pixel distribution of both PACT maps. *Top*: PACT tSZ noise power-spectrum (solid blue) compared with *Planck* and ACT noise power-spectrum (in dashed and dotted red lines) for the southern region (*left panel*) and the equatorial region (*right panel*). *Bottom*: same as the top but for the tSZ signal.

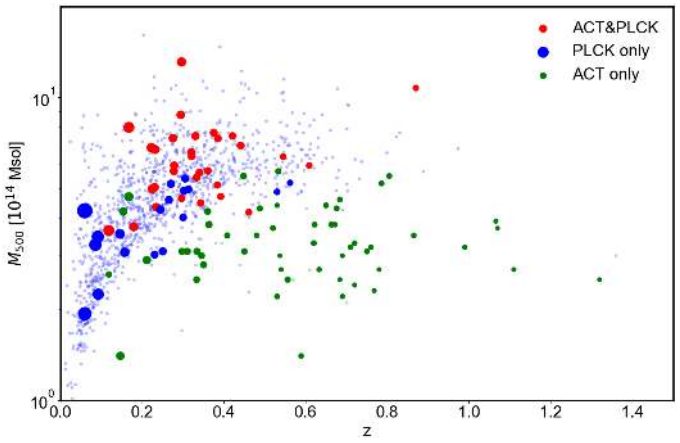

Fig. 6. Distribution in mass, in units of M_{500}, and in redshift of our sample (dots) compared with full *Planck* and ACT catalogs (light blue points). The colors indicate whether a cluster is detected by ACT (green dots), *Planck* (blue dots), or both (red dots). The size of the dots is proportional to the cluster size, Θ_{500}.

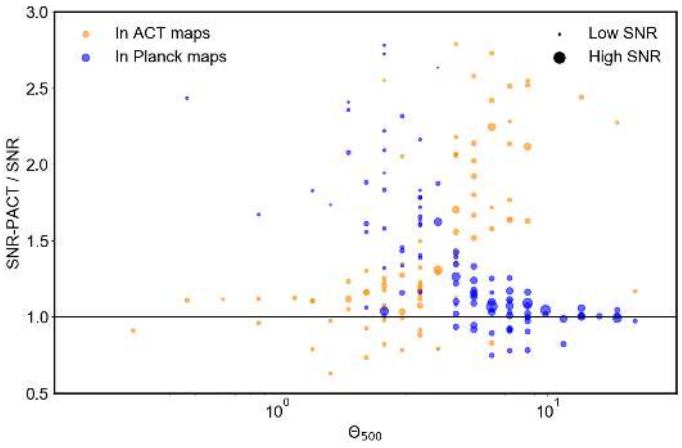

Fig. 7. Comparison of S/N values for clusters in ACT, *Planck,* and PACT maps as function of angular size. The ratio of the S/N obtained from PACT to the S/N obtained from the native ACT data (orange dots) or *Planck* data (blue dots) is plotted versus the angular size of the cluster. Each dot stands for one of the 119 clusters reported in *Planck* or ACT catalogs with size of symbol proportional to the PACT S/N.

from Hasselfield et al. (2013a) and the *Planck* catalogs from Planck Collaboration VIII (2011), Planck Collaboration XXIX (2014), Planck Collaboration Int. XXXII (2015) and Planck Collaboration XXVII (2016). We identify the clusters detected either only in the ACT data or only in the *Planck* survey. For these clusters, positions and native S/N values are those published by both experiments. We also identify the clusters detected both in ACT and in *Planck*. For these clusters, we chose the ACT position as a reference tSZ position given the higher resolution of this experiment.

Figure 6 shows the distribution of the 119 clusters considered in this study in the mass-redshift space. The cluster masses, M_{500}, are those reported in the ACT and *Planck* catalogs. Colors indicate whether a cluster is detected by ACT (green dots) or *Planck* (blue dots) or both (red dots) and size of the symbol is proportional to the angular size.

4.2. Significance of tSZ detections

For each cluster of the union sample displayed in Fig. 7 as a dot, we estimate the size, the flux, and the S/N at the reported positions using the MMF technique. We leave the discussion on the size-flux degeneracy to the next section and focus only on the S/N. The cluster properties are computed with the same MMF from the ACT data (orange dots) and *Planck* data (blue dots), that is two and six frequency channels, respectively, and from the PACT dataset, or the ensemble of eight frequency channels.

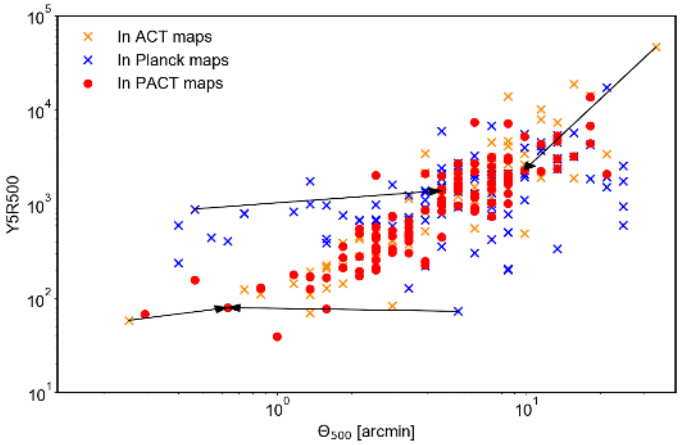

Fig. 8. Comparison of Y and Θ values for 119 tSZ clusters in ACT, *Planck,* and PACT maps. Arrows show how the size and flux change when estimated in native ACT or *Planck* maps only or when using the full PACT dataset.

We show in Fig. 7 ratio of the S/N obtained from PACT to the S/N obtained from the native dataset (ACT or *Planck*) with the same MMF as a function of the cluster size.

Figure 7 highlights the improvement on the detection of S/N both for extended clusters and more compact clusters, although a few clusters have a lower S/N when combining ACT and *Planck* data. We first notice that for most of the ACT and *Planck* clusters the S/N improves when we use the PACT combined data rather than the native ACT (*Planck*) data to estimate the S/N. The improvement can reach up to a factor three higher than the ACT (*Planck*) native S/N. In the case of ACT (orange dots), the highest improvements correspond to clusters with the largest sizes. In these cases, the PACT combination provides the large, angular scales of *Planck*, missing from the ACT data, which also filter out the CMB and astrophysical contamination. In the case of *Planck* (blue dots), the highest improvements in S/N are reached for clusters with small, angular sizes. The PACT dataset provides the small scales of ACT that are missing in *Planck* low-resolution data. For clusters with intermediate sizes, the average improvement in S/N induced by the use of the PACT dataset is on order of 50%. We also note from Fig. 7 that a few clusters (less than 10% of the full sample) exhibit smaller S/N values when the PACT dataset is used. Such a downward fluctuation of the S/N despite the use of more data was already noted. While the S/N improved for most SZ sources in the second *Planck* catalogue, about 23% had their S/N reduced below the detection limit of 4.5σ. These downward-fluctuated S/N were associated with weak detections likely to be Eddington-biased above the threshold. We note in the present analysis of the PACT dataset that the clusters with reduced S/N are ones of low significance. The modification of the background noise in the aggregated PACT dataset and the low significance of the tSZ detections result in downward-fluctuated detections. For the most nearby and thus extended clusters (such as A3395 at redshift $z = 0.05$), the background noise used in the MMF technique is overestimated due to the cluster signal at large scales. A dedicated MMF analysis of such extended sources would be needed.

4.3. Size and tSZ flux relation

The MMF method simultaneously adjusts the size, θ_{500}, and the integrated Compton parameter, Y_{500}, on the data. In Fig. 8 we show the tSZ flux and the size measured with the same MMF technique at the position of all the 119 clusters detected by ACT and *Planck* in the ACT footprint. The red dots show the outputs from the MMF applied to the combined PACT dataset. The orange and blue crosses are for MMF values obtained from the ACT and *Planck* data, respectively.

We first note the large dispersion in the $Y_{500}-\theta_{500}$ relation for the *Planck* case (blue crosses), which is due to the size-flux degeneracy. As was shown (Planck Collaboration VIII 2011; Planck Collaboration XXIX 2014), both quantities estimated simultaneously with the MMF filter are highly correlated. This degeneracy is particularly important in the case of low-resolution data such as *Planck* for which clusters are only marginally resolved. In the case of ACT (orange crosses), the resolution is much higher and the cluster sizes are better estimated, on average. We also note in Fig. 8, that the tSZ flux expressed in terms of the Y_{500} parameter can be overestimated both in *Planck* and in ACT. In the case of ACT, Y_{500} is overestimated for extended clusters. This is due to the fact that ACT lacks the large scales and is thus data are contaminated mostly by CMB and dust emission. In the *Planck* case, Y_{500} values are overestimated for small-size clusters unresolved by *Planck*. In addition, at the smallest sizes we notice that Y_{500} values show a plateau that is due to the noise in the *Planck* maps. We can see the same kind of plateau for the case of ACT but at lower amplitudes of noise.

When we use the combined PACT dataset for our MMF analysis (red dots) an improvement is induced over both ACT and *Planck* alone. This is triggered by the improved measurement of the sizes. Extended clusters in ACT benefit from the *Planck* large-scale signal and multiple frequency, which reduces the contamination and hence the Y_{500} estimate (orange crosses and arrows pointing to the left in Fig. 8). Unresolved clusters in *Planck* benefit from the small scales of ACT, which permits measurement of the cluster size and in turn the integrated Compton parameter Y_{500} (blue crosses and arrows pointing to the right in Fig. 8). Finally, for the smallest sizes the dominant contribution of the ACT data in the PACT combination reduces the noise level and further improves the tSZ estimates. The joint analysis of ACT and *Planck* with the MMF method hence reduces the size-flux degeneracy leading to a much smaller dispersion of the $Y_{500}-\theta_{500}$ relation.

4.4. tSZ profiles

We have shown in Sect. 3.2 that the combination of ACT and *Planck* channel maps allows us to reconstruct a PACT y-map that benefits on the one hand from the high resolution and low noise of ACT, and on the other hand from the large-scale modes and multiple frequencies of *Planck*. In this way, the reconstructed PACT y-map has better resolution, reduced noise, and astrophysical contamination. We now illustrate how the combined PACT map improves the measurement of the tSZ profile on individual clusters of galaxies.

Dedicated analyses by Crichton et al. (in prep.) and Santiago-Bautista et al. (in prep.) focus on the derived pressure profile from PACT data. Here, we select only four clusters with different angular sizes in order to exhibit the advantage of the combined PACT y-map over the independent use of ACT or *Planck* maps. Namely, we choose a nearby and very extended cluster: Abell 3158 at $z = 0.059$; a compact cluster that is smaller in size than the *Planck* beam: Abell 3404 at $z = 0.167$; an intermediately-high redshift cluster: PLCKESZ G262.71−40.9 at $z = 0.421$; and finally a high redshift cluster at the resolution limit of *Planck*: ACT-CL J0546−5345 at redshift $z = 1.066$.

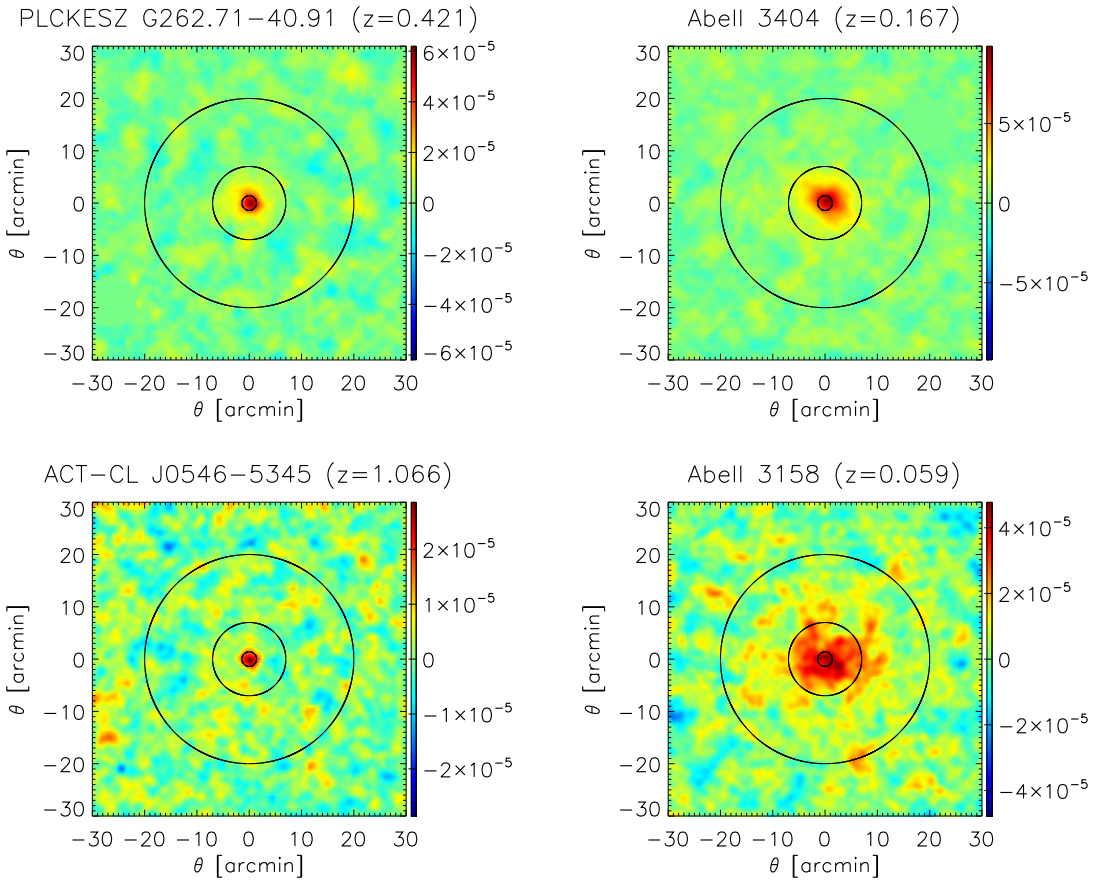

Fig. 9. Cut-outs of tSZ signal from reconstructed PACT y-map for four selected galaxy clusters. The innermost black circle is for 1.4 arcmin (ACT resolution), the middle black circle represents the *Planck* resolution of 7 arcmin, and the outer black circle is drawn for a radius of 20 arcmin.

In Fig. 9, we show the tSZ 1° × 1° patch from the PACT y-map, centered at the cluster position for each cluster. The black circles displayed in the images are drawn for radii of 1.4, 7, and 20 arcmin, from the innermost to the outermost circles. The associated radial Compton parameter profiles, derived from the PACT y-map, are shown in Fig. 10 as black lines. We also plot the profiles obtained from the *Planck* y-map (blue lines) together with those obtained from the high-pass filtered ACT-148 GHz map (red lines). The high-pass filter, applied only for this figure, removes the ACT background noise to better emphasize how the different datasets provide information at different scales (in this case ACT contributing at small scales). The filtering induces fluctuations observed in the cluster profiles. Figure 9 exhibits the complementarity in PACT of both ACT and *Planck* data, respectively, which is particularly well illustrated in the upper right panel where the smallest-scale tSZ signal is provided by ACT and the outskirt of the tSZ signal by *Planck*.

5. Conclusion

We have built a composite dataset from the ACT and *Planck*-HFI channel maps and their associated noise maps. This dataset was used to perform an optimized reconstruction and extraction of the tSZ signal. In practice, we followed two approaches. The first one is source-oriented and hence focused on the detection of tSZ clusters using an MMF detection method. The second approach is based on the reconstruction of a tSZ y-map using an ILC technique. For either approach, we have shown that the composite PACT dataset benefits from the high resolution of ACT and the large-scale modes and large number of frequency channels of *Planck*.

For the tSZ cluster detection, we have shown that we recover all clusters detected in the individual datasets of *Planck* and ACT. In addition, we detect new tSZ sources some of which associated with bona-fide clusters at redshifts up to 0.93. These sources were neither reported by *Planck* nor by ACT independently. We have also shown that the combination of ACT and *Planck* data reduces the size-flux degeneracy and improves the S/N of detected clusters by up to a factor three with respect to their native ACT or *Planck* S/N.

For the Compton y parameter map, we used a scale-dependent optimization of the reconstructed tSZ signal with respect to noise and foreground residuals. We have shown that the resulting PACT y-map reproduces the tSZ signal from arcminute angular scales present in ACT data to the largest angular scales captured by *Planck*. The improvement in the reconstructed tSZ PACT map was also illustrated by the derived Compton y profiles for representative clusters, showing the complementarity of ACT and *Planck* in reproducing both the inner structure and outskirts of the pressure profile. This new PACT y-map will be used for further analysis of the pressure profiles and hot gas distribution in individual structures.

This first optimal combination of multifrequency and mutli-experiment data illustrates the advantages of data aggregation for tSZ studies. With the forthcoming increase of publicly available data (e.g., ACTpol, AdvACT, SPTpol, and SPT3G), joint studies will allow a synoptic analysis of tSZ over the majority of the extragalactic sky.

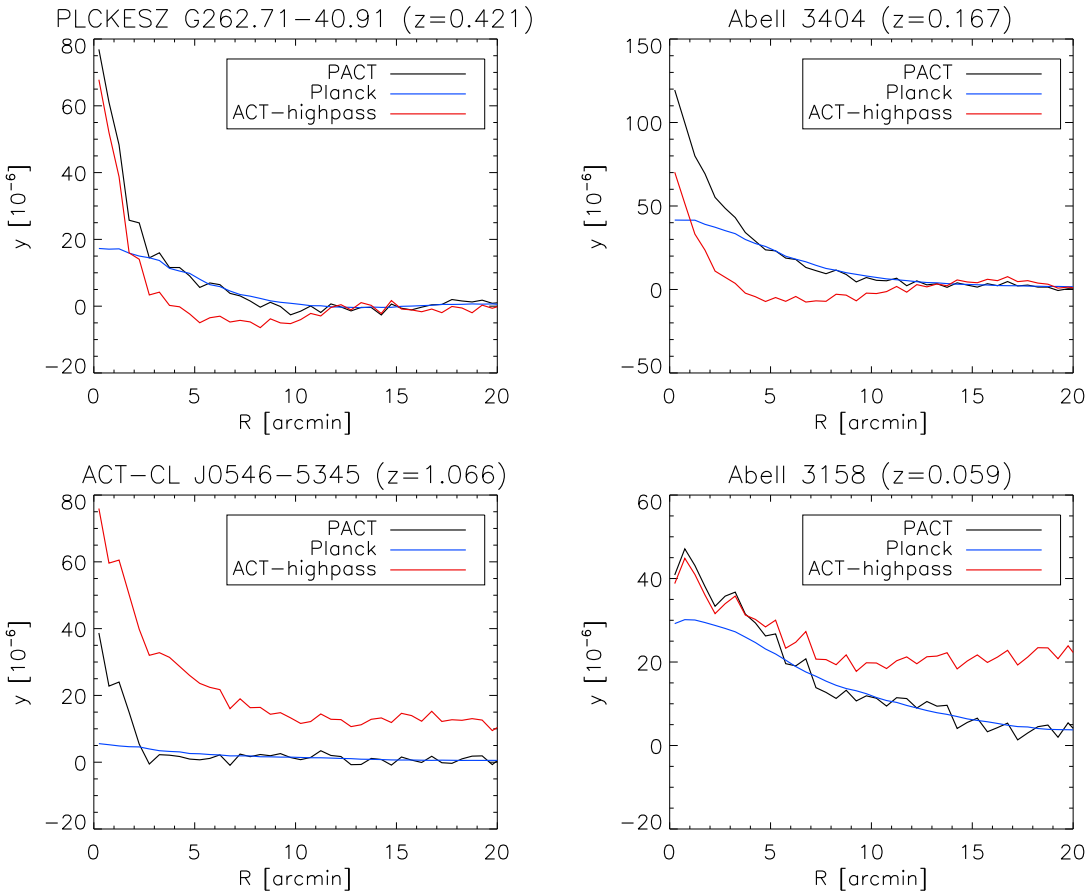

Fig. 10. Comparison of the radial tSZ profiles for four clusters in Fig. 9. Profiles were obtained from the PACT y-map (black), from the *Planck* y-map (blue), and the 148 GHz-ACT high-pass filtered map (red).

Acknowledgements. The authors thank an anonymous referee for useful comments. This research was performed in the context of the ISSI international team project "SZ clusters in the *Planck* era" (P.I. N. Aghanim and M. Douspis). The authors acknowledge partial funding from the DIM-ACAV and the Agence Nationale de la Recherche under grant ANR-11-BS56-015. The research leading to these results has received funding from the European Research Council under the H2020 Programme ERC grant agreement no 695561. JMD acknowledges support from project AYA2015-64508-P (MINECO/FEDER, UE) funded by the Ministerio de Economia y Competitividad. DC acknowledges support from the South African Radio Astronomy Observatory, which is a facility of the National Research Foundation, an agency of the Department of Science and Technology. The development of *Planck* has been supported by: ESA; CNES, and CNRS/INSU-IN2P3-INP (France); ASI, CNR, and INAF (Italy); NASA and DoE (USA); STFC and UKSA (UK); CSIC, MICINN, JA, and RES (Spain); Tekes, AoF, and CSC (Finland); DLR and MPG (Germany); CSA (Canada); DTU Space (Denmark); SER/SSO (Switzerland); RCN (Norway); SFI (Ireland); FCT/MCTES (Portugal); and PRACE (EU). This research has made use of the following databases: the NED and IRSA databases, operated by the Jet Propulsion Laboratory, California Institute of Technology, under contract with the NASA; SIMBAD, operated at CDS, Strasbourg, France; SZ cluster database (`szcluster-db.ias.u-psud.fr`) operated by Integrated Data and Operation Center (IDOC), which is operated by IAS under contract with CNES and CNRS. This research made use of Astropy, the community-developed core Python package.

References

Aghanim, N., Hurier, G., Diego, J.-M., et al. 2015, A&A, 580, A138
Arnaud, M., Pratt, G. W., Piffaretti, R., et al. 2010, A&A, 517, A92
Birkinshaw, M. 1999, Phys. Rep., 310, 97
Bleem, L. E., Stalder, B., de Haan, T., et al. 2015, ApJS, 216, 27
Bobin, J., Moudden, Y., Starck, J.-L., Fadili, J., & Aghanim, N. 2008, Stat. Methodol., 5, 307
Bobin, J., Sureau, F., Starck, J.-L., Rassat, A., & Paykari, P. 2014, A&A, 563, A105
Bobin, J., Sureau, F., & Starck, J.-L. 2016, A&A, 591, A50
Carvalho, P., Rocha, G., & Hobson, M. P. 2009, MNRAS, 393, 681
Carvalho, P., Rocha, G., Hobson, M. P., & Lasenby, A. 2012, MNRAS, 427, 1384
Chown, R., Omori, Y., Aylor, K., et al. 2018, ApJS, 239, 10
Crawford, T. M., Chown, R., Holder, G. P., et al. 2016, ApJS, 227, 23
Dünner, R., Hasselfield, M., Marriage, T. A., et al. 2013, ApJ, 762, 10
Hasselfield, M., Hilton, M., Marriage, T. A., et al. 2013a, JCAP, 7, 008
Hasselfield, M., Moodley, K., Bond, J. R., et al. 2013b, ApJS, 209, 17
Herranz, D., Gallegos, J., Sanz, J. L., & Martínez-González, E. 2002, MNRAS, 334, 533
Hilton, M., Hasselfield, M., Sifón, C., et al. 2018, ApJS, 235, 20
Hurier, G., Macías-Pérez, J. F., & Hildebrandt, S. 2013, A&A, 558, A118
Marriage, T. A., Acquaviva, V., Ade, P. A. R., et al. 2011, ApJ, 737, 61
Melin, J. B., Bartlett, J. G., & Delabrouille, J. 2006, A&A, 459, 341
Nagai, D., Vikhlinin, A., & Kravtsov, A. V. 2007, ApJ, 655, 98
Piffaretti, R., Arnaud, M., Pratt, G. W., Pointecouteau, E., & Melin, J.-B. 2011, A&A, 534, A109
Planck Collaboration VIII. 2011, A&A, 536, A8
Planck Collaboration XXI. 2014, A&A, 571, A21
Planck Collaboration XXIX. 2014, A&A, 571, A29
Planck Collaboration VII. 2016, A&A, 594, A7
Planck Collaboration VIII. 2016, A&A, 594, A8
Planck Collaboration XXII. 2016, A&A, 594, A22
Planck Collaboration XXIII. 2016, A&A, 594, A23
Planck Collaboration XXVII. 2016, A&A, 594, A27
Planck Collaboration I. 2019, A&A, in press, `https://doi.org/10.1051/0004-6361/201833880`
Planck Collaboration Int. XXXII. 2015, A&A, 581, A14
Remazeilles, M., Delabrouille, J., & Cardoso, J.-F. 2011, MNRAS, 418, 467
Remazeilles, M., Aghanim, N., & Douspis, M. 2013, MNRAS, 430, 370
Rykoff, E. S., Rozo, E., Busha, M. T., et al. 2014, ApJ, 785, 104
Staniszewski, Z., Ade, P. A. R., Aird, K. A., et al. 2009, ApJ, 701, 32
Swetz, D. S., Ade, P. A. R., Amiri, M., et al. 2011, ApJS, 194, 41
Wen, Z. L., & Han, J. L. 2015, ApJ, 807, 178
Zeldovich, Y. B., & Sunyaev, R. A. 1969, Ap&SS, 4, 301